nature communications

Article

https://doi.org/10.1038/s41467-025-61794-y

Artificial-intelligence-guided design of ordered gas diffusion layers for high-performing fuel cells via Bayesian machine learning

Received: 22 October 2024

Accepted: 25 June 2025

Jing Sun[1,3], Pengzhu Lin[1,3], Lin Zeng[2], Zixiao Guo[1], Yuting Jiang[1,2], Cailin Xiao[2], Qinping Jian[1], Jiayou Ren[1], Lyuming Pan[2], Xiaosa Xu[1], Zheng Li[1,2], Lei Wei[2] & Tianshou Zhao[1,2] ✉

Rational design of gas diffusion layers (GDL) is an example of a long-standing pursuit to increase the power density and reduce the cost of proton exchange membrane fuel cells (PEMFC). However, current state-of-the-art GDLs are designed by trial-and-error, which is a time-consuming endeavor. Here, we propose a closed-loop workflow of Bayesian machine learning approach to guide the design of GDL structures. With artificial neural network accelerating the calculation of anisotropic transport properties of reconstructed GDLs, Bayesian optimization algorithm identifies optimal structures in only 40 steps, maximizing the PEMFC's limiting current density. Results suggest that the optimal porous GDL structure consists of highly orientated fibers with moderate diameters, which is successfully fabricated with a controlled electrospinning technique. The PEMFC demonstrates a high power density of 2.17 W cm^{-2} and a limiting current density of ~7200 mA cm^{-2}, far exceeding that with commercial GDL (1.33 W cm^{-2} and ~2700 mA cm^{-2}).

To achieve net-zero emission (NZE) targets, producing green hydrogen through water electrolysis powered by renewable energy is seen as a promising solution to address carbon emissions[1]. The NZE Scenario by 2030 forecasts that nearly 8 Mt of hydrogen will be utilized in transportation. Proton exchange membrane fuel cells (PEMFCs) represent the primary devices employed to convert hydrogen into electricity, primarily in heavy-duty vehicle applications due to their higher energy density and refueling advantages over battery electric vehicles[2,3]. Beyond mobile applications, the roadmap from renewable electricity to hydrogen via electrolyzers and back to electricity through fuel cells underscores the crucial role of PEMFCs in stationary energy storage applications or for distributed/back-up power[4]. However, the industrial implementation is heavily dependent on the reduction of the cost and its operation stability[5]. To meet the cost and durability targets set by the United States Department of Energy for light-duty vehicles ($30 per kW and 8000 h) and heavy-duty vehicles ($60 per kW and 30,000 h), respectively[6,7], it is imperative that the power density of PEMFCs be significantly advanced. This necessitates meeting ambitious targets, such as the 2.5 W cm^{-2} goal set by the New Energy and Industrial Development Organization of Japan[8], by the year 2030.

Enhancing the power density of PEMFC demands reducing three types of losses: activation, ohmic, and mass transport losses. Over recent decades, advances in catalyst and membrane electrode assembly (MEA) design have significantly reduced activation loss[9,10], but research on tackling mass transport issues, specifically "water flooding" at high current densities, is not keeping pace. When liquid water accumulates in the pores of catalyst layer (CL), it blocks the transport pathways for oxygen to reach the reactive sites[11],

---

[1]Department of Mechanical and Aerospace Engineering, The Hong Kong University of Science and Technology, Kowloon, China. [2]Department of Mechanical and Energy Engineering, Southern University of Science and Technology, Shenzhen, China. [3]These authors contributed equally: Jing Sun, Pengzhu Lin. ✉e-mail: zhaots@sustech.edu.cn

deteriorating the fuel cell performance with reduced power density and limiting current density (LCD)[12] (Supplementary Fig. 1). Excess water content in the cell also negatively affects the durability of PEMFCs[13]. Nevertheless, the issue of water flooding remains an intricate and poorly understood multi-phase transport phenomenon.

The transport of liquid water is driven by capillary force in porous media, and the two-phase transport phenomenon is significantly influenced by the geometric structure and wettability of the gas diffusion layer (GDL) and microporous layer (MPL)[14,15]. However, the randomly connected fibers of the GDL lead to nondirectional and tortuous pathways for water transport, resulting in the accumulation of water in the pores, which blocks the gas transport. Modifying the structures (e.g., constructing perforations[16,17]) and tuning wettability are typical strategies adopted to boost water drainage, despite the recent advance in proposing a GDL-less configuration with electrode-flow field integration[18]. For example, the geometric parameters of perforations on carbon paper are systematically optimized, such as density, length, and width[19]. In addition, constructing patterned wettability[20,21], water highways[22] by introducing both hydrophilic and hydrophobic regions in GDL regulated the pathways for gas/water transport. However, the erratic paths still exist in these modified GDLs, and their water removal capability under high current density (e.g., >5 A cm^{-2}) is yet to be validated[23].

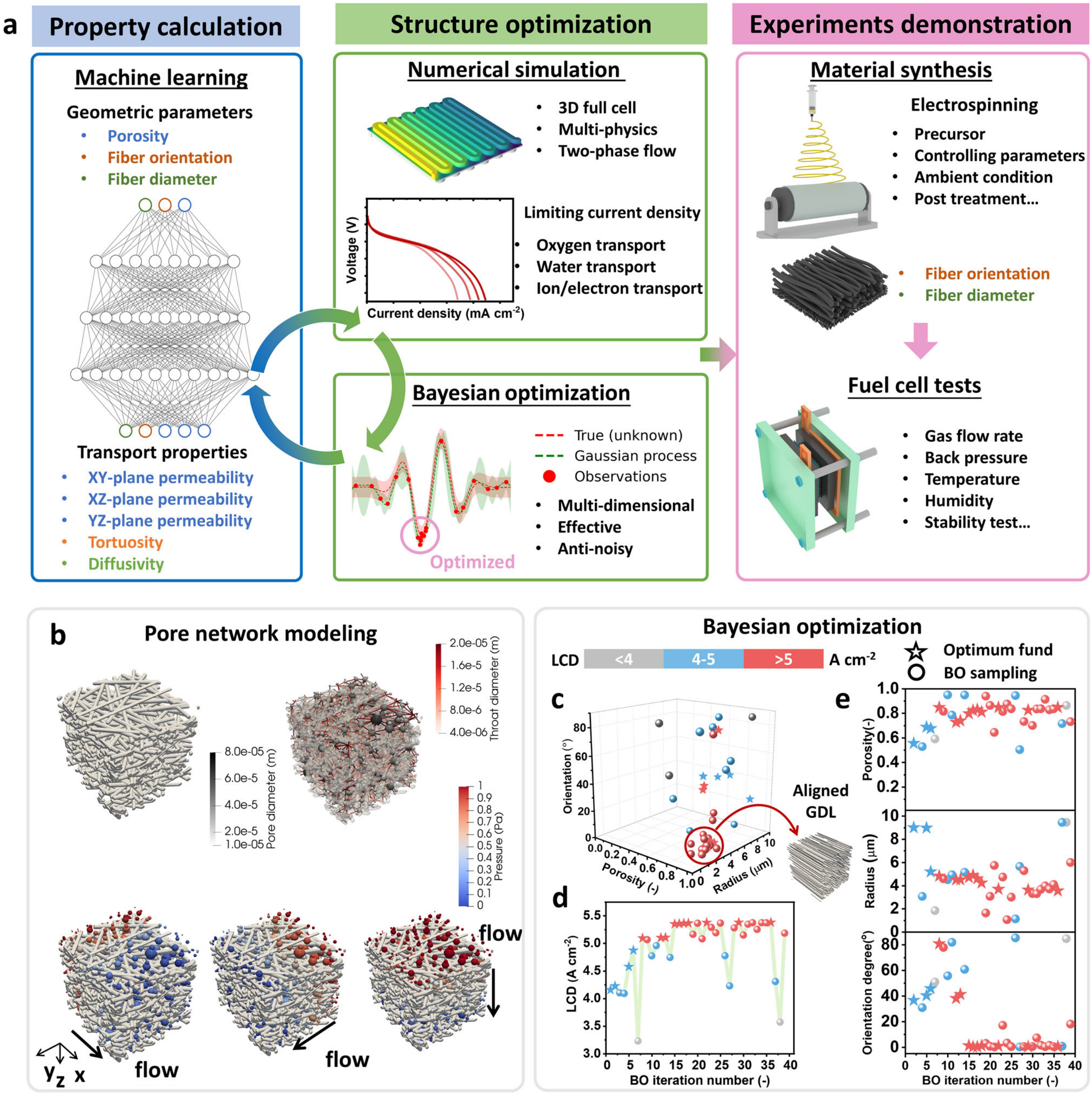

Fig. 1 | Introduction of Artificial Intelligence (AI)-guided design and fabrication of fiber-based gas diffusion layer (GDLs). a Workflow of closed-loop Bayesian machine learning which integrates calculation of anisotropic transport properties of GDLs using machine learning, numerical simulation incorporating pore-scale modeling with cell-scale simulation, and Bayesian optimization. Optimized GDL is synthesized with a controlled electrospinning method and evaluated through fuel cell tests under different testing conditions. **b** Pore network modeling to calculate anisotropic transport properties. Bayesian optimization (BO) process including **c**, **d** optimum fund and BO sampling with limiting current density (LCD) as an indicator. Corresponding geometric properties including fiber porosity, diameter, and orientation are mapped in **e**. Source data are provided as a Source Data file.

More significantly, it is reported that water tends to aggregate in the under-rib region in the GDL to flow channel configuration, as evidenced by X-ray imaging and modeling[24,25], which limits the efficacy of modifications on existing carbon paper GDLs. Efforts have been made to tackle the under-rib water accumulation. For example, deterministic perforations that connect channels and ribs are proven to facilitate water removal[8] and the adoption of patterned GDL, such as carbon cloth, can better alleviate in-plane water accumulation over carbon paper-based GDLs. In addition, Csoklich et al. adopted woven fabrics (gold-sputtered polyethylene) with a deterministic structure with improved transport properties for gas/water transport[26]. However, the trial-and-error optimization of GDLs based on existing structures and materials is ineffective and laborious in searching for the best structures from numerous structures with varied geometric properties.

Artificial intelligence (AI) and machine learning (ML) are powerful tools for solving complex problems. ML has shown advantageous performance over trial-and-error experiments in tasks such as predicting material properties[27], optimizing electrode manufacturing[28], and analyzing three-dimensional pore structures[29]. ML has been applied across various PEMFC components, including electrocatalysts[30], membrane[31], channels[32], and GDLs[33]. For example, Li and Liu et al. applied AI-aided models to design nonprecious metal electrocatalysts and achieved good accuracy for improving the efficiency of MEA design. ML has been applied to optimize the properties of proton exchange membranes, emphasizing the role of ML models in predicting membrane performance and durability. In addition, there are several trials to adopt ML to optimize the GDL microstructures. A multi-objective optimization method was developed for the design of GDL microstructure for improving several key properties of GDL microstructure by searching manufacturing parameters[33]. Besides, a Bayesian optimizer was developed for optimization of the microstructure of carbon felt electrodes combined with the lattice Boltzmann method[34]. In addition to pore-scale optimization, there are explorations to optimize the GDL parameters, such as porosity and thickness, in the cell-scale models[35,36]. However, the task of searching for the best GDL structures involves complex multi-scale and multi-physics modeling. This includes intricate pore-scale modeling linking geometric structure to transport properties, and performance assessment in cell-scale multi-physics modeling, making the optimization over a library of structures a significant challenge. Therefore, it is necessary to develop an efficient optimization strategy that integrates multi-scale and multi-physics modeling.

In this study, we propose a closed-loop design of GDL via multi-scale modeling coupling Bayesian ML in a three-step workflow. As shown in Fig. 1, ML is employed to expedite the calculation of anisotropic transport properties of GDLs. An Artificial Neural Network (ANN) with independent input parameters (porosity, fiber orientation, and fiber radius) is trained on a comprehensive dataset constructed by pore network modeling, which significantly reduces the computational cost of the time-consuming pore-scale modeling. The anisotropic transport properties are incorporated into the three-dimensional two-phase multi-physics cell-scale model to evaluate cell performance, with the LCD as the key descriptor for optimization. Bayesian optimization (BO), a powerful tool for multidimensional optimization of expensive, difficult-to-evaluate, or noisy functions/tasks, serves as an effective approach for optimizing the key geometric parameters of GDLs by maximizing the LCD of PEMFC. The link between microstructure and cell performance is effectively established by integrating pore-scale with cell-scale modeling, which is combined with ANN and BO in a closed-loop workflow for rapid, low-cost optimization (Supplementary Fig. 2). The optimization results suggest that optimal porous GDLs consist of highly orientated fibers of moderate diameters. The aligned GDL is fabricated using an electrospinning method with designed precursor solutions and properly adjusted conditions, which are assessed in PEMFC tests with a comprehensive study on the influence of geometric parameters and the cell operating conditions. When the aligned fibers are placed connecting the channels and ribs, water can continuously be transferred from CL to the flow field along the through-plane direction and be fast removed along the in-plane direction, resulting in enhanced PEMFC performances over existing carbon paper-based GDLs.

Results

Optimal GDL structure predicted by Bayesian optimization

The first step in the workflow is the property calculation of fiber-based GDLs, which are reconstructed from key features (porosity, fiber diameter and orientation) (Supplementary Fig. 3). Anisotropic transport properties, including permeability, tortuosity, and diffusivity are determined using pore network modeling, where the equivalent pores and throats are extracted based on complex porous structure and followed by Stokes flow simulation in x, y, z directions, as shown in Fig. 1b. However, case-by-case determination of the transport properties is time-consuming and laborious. To accelerate the property calculation process, an ANN is developed as shown in Fig. 1a, with the input of three key features and five output transport properties. The ANN is carefully trained to avoid overfitting and accurately capture the anisotropic transport properties of complex porous structures, with an R-squared of 0.98 in prediction (Supplementary Fig. 4, 5). The unique GDL structure represented by mass transport properties is evaluated in a 3D PEMFC multi-physics model (Supplementary Fig. 6), with LCD used as the descriptor for representing the overall cell-scale performance, which is given by:

$$i_{\mathrm{lim}} = \arg\max_{i}(E_{\mathrm{cell}} = E_{\mathrm{rev}} - E_{\mathrm{act}} - E_{\mathrm{Ohm}} - E_{\mathrm{con}} \rightarrow 0) \tag{1}$$

where i_{lim} represents the current density of fuel cells approaching zero operating voltage, caused by polarization by activation, ohmic, and concentration loss.

BO algorithm integrates pore-scale property calculation of GDLs and cell-scale numerical simulation of fuel cells to speed up the search for optimal GDL structures. The algorithm is given by:

Algorithm 1. Bayesian Optimization

```
Input: Objective function $f$, domain $\chi$, initial observation $D_0$
Output: The best input $x^* \in \chi$ and its function values $f(x^*)$
Initialize Gaussian Process (GP) with prior $p(f)$
Define acquisition function $\alpha(x; D)$
$D \leftarrow D_0$
for t = 1,2, …, T do
    Select $x_t \in \chi$ by optimizing the acquisition function:
        $x_t = \arg\max_{x \in \chi} \alpha(x; D)$
    Evaluate the objective function $y_t = f(x_t)$ by multi-scale modeling:
        1. Pore-scale calculation of GDLs
        2. Cell-scale simulation of fuel cells
    Augment the data: $D \leftarrow D \cup \{(x_t, y_t)\}$
    Update the GP model with the new data $D$
end for
$x^* \leftarrow \arg\max_{x \in \chi} f(x)$ based on the GP posterior
return $x^*, f(x)$
```

BO is used to maximize the LCD with the objective function by multi-scale modeling, within the domain (χ) of porosity, pore radius, and fiber orientation. During each iteration in the BO algorithm, we employed the acquisition function for selecting the next x_t, evaluated the objective function and updated the Gaussian process model, to progressively approach the global optimum for complex fuel cell simulations. Figure 1c, d shows the convergence of optimum LCD within 40 iterations, where the optimal structures mainly lie in the regions with porosity in the range of 0.7–0.9, fiber radius of 3–6 μm,

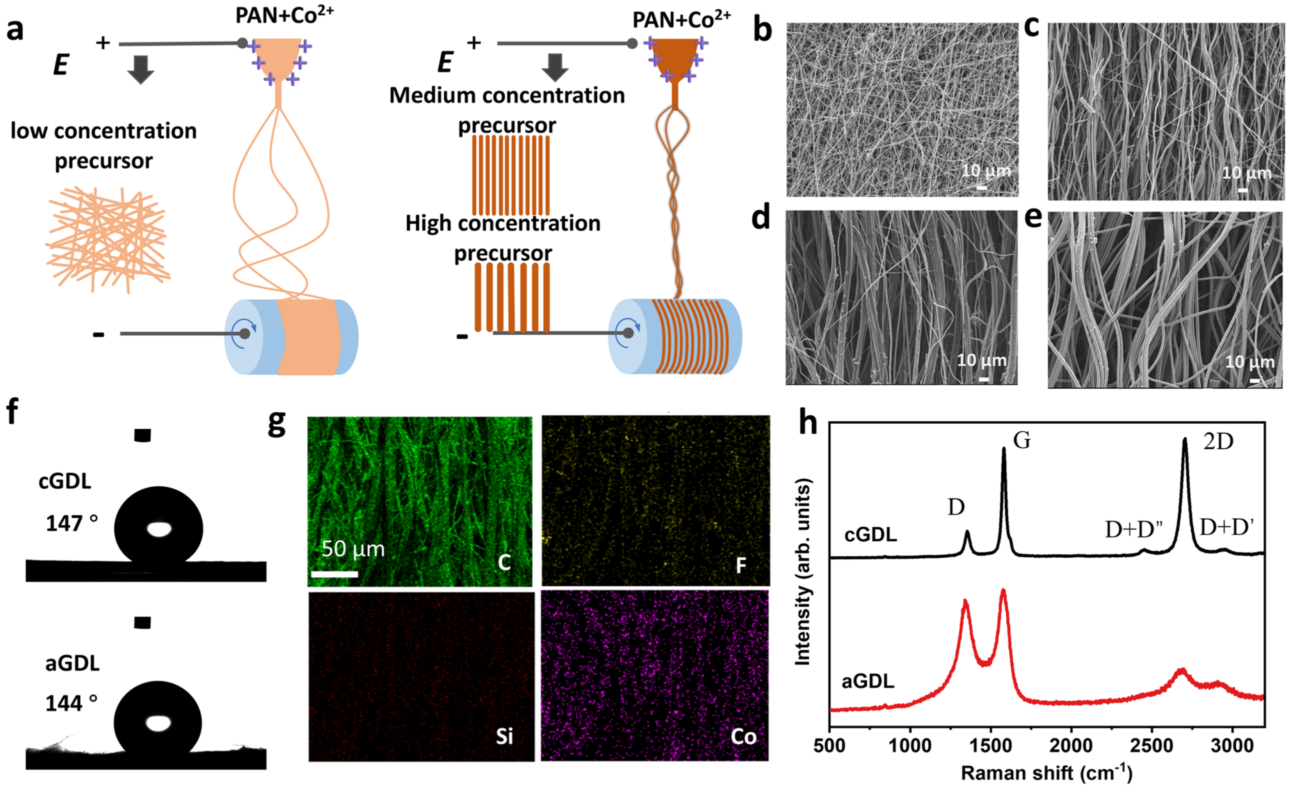

Fig. 2 | Synthesis and material characterization of the electrospun gas diffusion layer (GDL). a Schematic illustration of electrospinning jets for the formation of dense and random fibers and aligned fibers. *E*, applied voltage. Scanning electron microscopy (SEM) images of the carbon fiber mat derived from **b** 8 wt%, **c** 11 wt%, **d** 13 wt% and **e** 15 wt%, which are respectively repeated with the same structures over three times. **f** Contact angle of commercial GDL (cGDL) and aligned GDL (aGDL) after hydrophobicity treatment. **g** Energy-dispersive X-ray spectroscopy (EDS) mapping of the treated aGDL. **h** Raman spectra of aGDL and cGDL. Source data are provided as a Source Data file.

and a fiber orientation near 0°, representing a highly aligned fiber structure (Fig. 1e) with the reconstructed structure as a representative. However, fabricating aligned carbon fiber electrodes remains challenging, as fiber-fabricating techniques like wet-spinning and melt-spinning typically result in fibers with diameters much larger than 10 µm and poorly adjusted fiber orientation, and traditional electrospinning technique is commonly used for fabricating nanoscale fibers that are randomly dispersed.

Synthesis and characterization of ordered GDL

To obtain the optimal GDL structure, we developed a controlled electrospinning method to fabricate aligned GDLs with different fiber diameters. Polyacrylonitrile (PAN) and cobalt salt are dissolved in DMF solutions to form the precursor solution for electrospun MPL and GDL. The addition of cobalt salt can facilitate the formation of aligned fibers during the electrospinning process[37–39], and later can be reduced to cobalt particles and catalyze the graphitization of carbon fibers[40,41]. The small amount of Co particles in GDLs is well wrapped inside the fiber or a layer of graphitized carbon (Supplementary Figs. 7, 8), which will not influence PEMFC performance. The fabrication of the dense polymer mat for MPL and aligned polymer fiber mat with a relatively large fiber diameter for GDLs is achieved by adjusting the concentration of precursor solution and electrospinning conditions. As shown in Fig. 2a, a low PAN concentration (e.g., 8 wt%) is used to derive MPL, which exhibits relatively low viscosity. Under the high voltage, the ejected jet becomes highly dispersed, rendering the formation of thin fibers that randomly land on the collecting drum. After stabilization and carbonization, the as-synthesized MPL shows a dense morphology (Fig. 2b), with a fiber diameter in the range of 400–1000 nm (Supplementary Fig. 9) that is randomly displaced. When increasing PAN concentration (e.g., 11, 13, and 15 wt%), the viscosity of the precursor solution increases, and the jet tends to stick together and form standing fiber bundles, as shown in Fig. 2a. Under this condition, the concentrated fiber jets land on the collector in a fixed position and interweave into the aligned fibrous morphology, as shown in Fig. 2c-e. It is also worth pointing out that the fiber diameter increases with increased PAN concentration. As measured from the magnified figures (Supplementary Fig. 10), the diameter of aligned carbon fiber derived from the precursor solution with 11, 13, and 15 wt% PAN is ~3, ~6, and ~10 µm, respectively. Carbon fibers which are heat treated at 1100 °C typically shows a relatively poor hydrophobicity, with the contact angle measured to be below 120° (Supplementary Fig. 11). The subsequent hydrophobic treatment using 1H,1H,2H,2H-Perfluorooctyltriethoxysilane (PFTS)/ethanal solution is critical in increasing the hydrophobicity which significantly increases the contact angle to around 144°, which is comparable to that of the commercial GDLs (~147°), as shown in Fig. 2f. Compared with the fibers without hydrophobicity treatment, the morphologies of the fibers after treatment remain almost the same (Supplementary Fig. 12). The energy-dispersive X-ray spectroscopy (EDS) mapping shows that the hydrophobic product is uniformly distributed on the fiber surface, as evidenced by the appearance of uniformly distributed F and Si element (Fig. 2g and Supplementary Fig. 13)[42]. The carbonization and graphitization degree of the as-synthesized GDL is compared with the commercial ones using Raman spectroscopy[43]. As shown in Fig. 2h, the commercial GDL (cGDL) which is typically graphitized at temperature over 2000 °C[44,45] shows a relatively high graphitization degree, with sharp peaks corresponding to G band and G′ (or 2D) band visible at the Raman shift of around ~1580 and ~2700 cm^{-1}, respectively. In comparison, the graphitization degree of home-made electrode is slightly inferior to the commercial ones with a relatively high peak intensity of disordered carbon (D band) at ~1350 cm^{-1}, since only a carbonization at

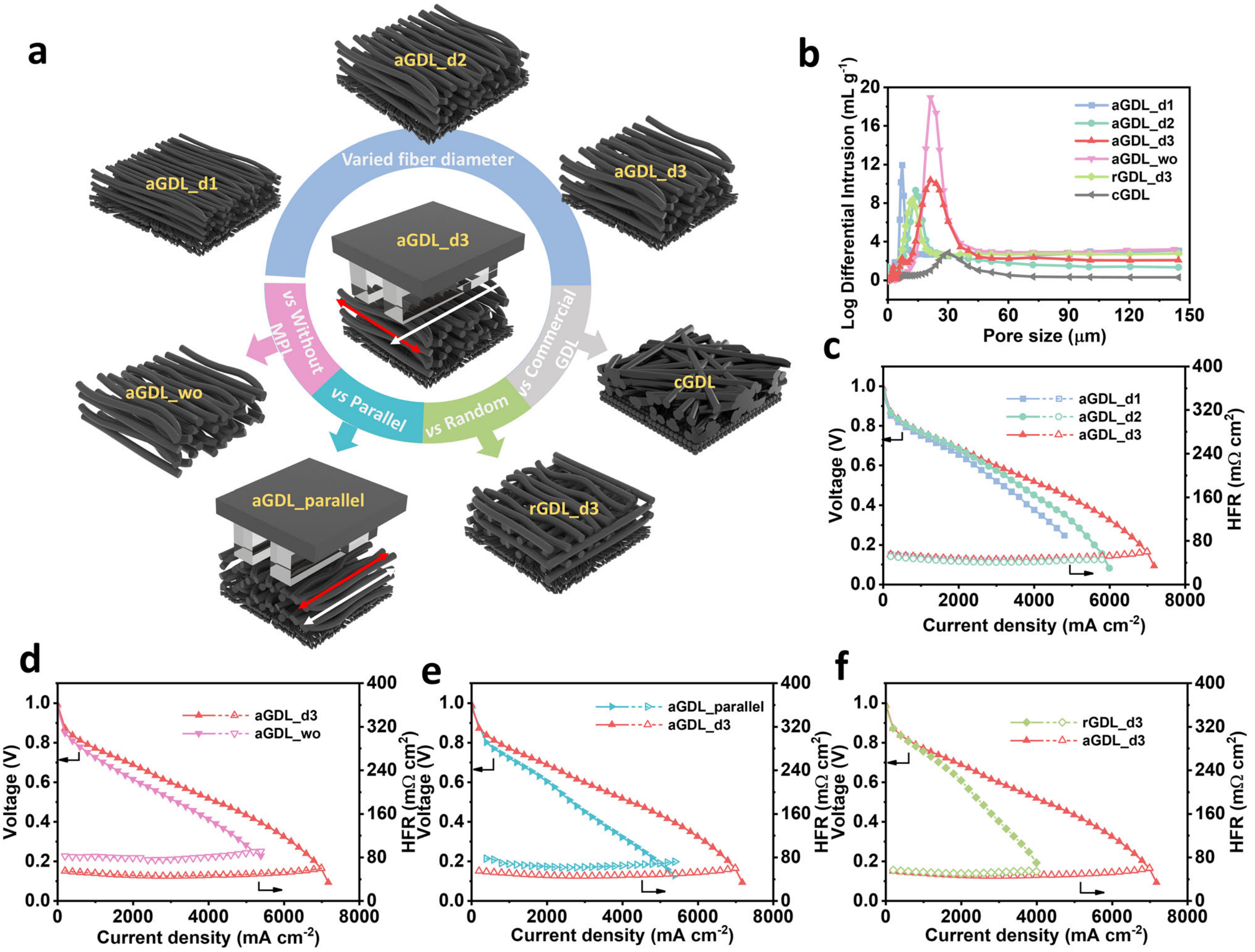

Fig. 3 | Influence of gas diffusion layer (GDL) structure and placing configurations on proton exchange membrane fuel cell (PEMFC) performance. **a** Schematics of GDLs with different structures and arrangements. **b** Mercury intrusion porosimetry (MIP) characterized pore size distribution of different GDLs. Performance comparison (polarization curve and HFR) between PEMFCs with GDLs of **c** different fiber diameter, **d** with/without microporous layer (MPL), **e** different placing orientation with respect to flow field and **f** aligned vs. random fibers. The operating condition of (**c**–**f**) is under the standard testing condition in our study with a back pressure of 150 kPa, stoichiometric number of 3/3 and a minimum rate of 0.5/0.5 NL min^{-1} of H_2/air, 100% humidity, and 80 °C. HFR, high-frequency resistance. Arrows in (**c**–**f**) indicate the corresponding y-axes for the different curves. All the voltage is not iR corrected. Source data are provided as a Source Data file.

1100 °C is adopted during the heat treatment process. Supplementary Fig. 14 illustrates three-dimensional morphology of GDLs from computed tomography (CT) results. The rendering results reveal that aligned GDL (aGDL) exhibits well-aligned fibers and interconnected pores, whereas cGDL displays random pores within the stochastic fibers and uneven pore distribution. The pore size distributions of GDLs are further analyzed based on CT results using pore network algorithms, showing that the equivalent pore diameter of aGDL is larger than that of cGDL and has distributions over a wider range.

GDL structure optimization with orthogonal experiments

With the proposed strategy to synthesize MPL and different GDLs, we systematically investigated the influence of the GDL fiber diameter, with/without MPL, the aligned fiber orientation with respect to the flow field, and fiber randomness, on PEMFC performance. As illustrated in Fig. 3a, three GDLs named as aGDL_d1, aGDL_d2, and aGDL_d3 are respectively derived from PAN precursors of concentration of 11, 13, and 15 wt%, and stack with MPL. The aGDL_wo is free of MPL and has the same aligned GDL (aGDL_d3). With the aGDL_d3, we further compared two arrangements relative to the flow channels, one is placing the aGDL vertical to the flow channel and the other is placing the aligned GDL in parallel to the flow channels, which we name the latter as aGDL_parallel. To compare the aligned GDL with its randomly arranged counterpart without involving the influence of other factors, such as varied fiber diameter, we stack several thin layers of aligned GDLs in different orientations, as shown in Supplementary Figs. 15 and 16, and get rGDL_d3. Lastly, the aGDLs are compared with commercial PTFE-treated carbon paper-based GDLs that are coated with particle-based MPL. With all these GDLs, the pore structures are characterized by mercury intrusion porosimetry (MIP), as shown in Fig. 3b. It is found that the as-prepared aGDL_d3 exhibits large pores in the same range as commercial GDL, which are around 30 μm. When varying the fiber diameter of the GDL, the pore size decreases in the sequence that aGDL_d1<aGDL_d2 <aGDL_d3. It is worth noting that rGDL_d3 fabricated by altering the placement between different layers of aligned fibers exhibits a reduced pore size as compared to that of aGDL_d3.

The influence of fiber diameter of aligned GDLs is shown in Fig. 3c. Due to the limitation of electrospinning technique in fabricating micro-scale fibers, the upper limit of the fiber diameter is ~10 μm. The HFR curves for the three cells almost overlap, indicating comparable ohmic losses. Variations in the polarization curves primarily occur in the mass transport loss dominant region, while the activation and

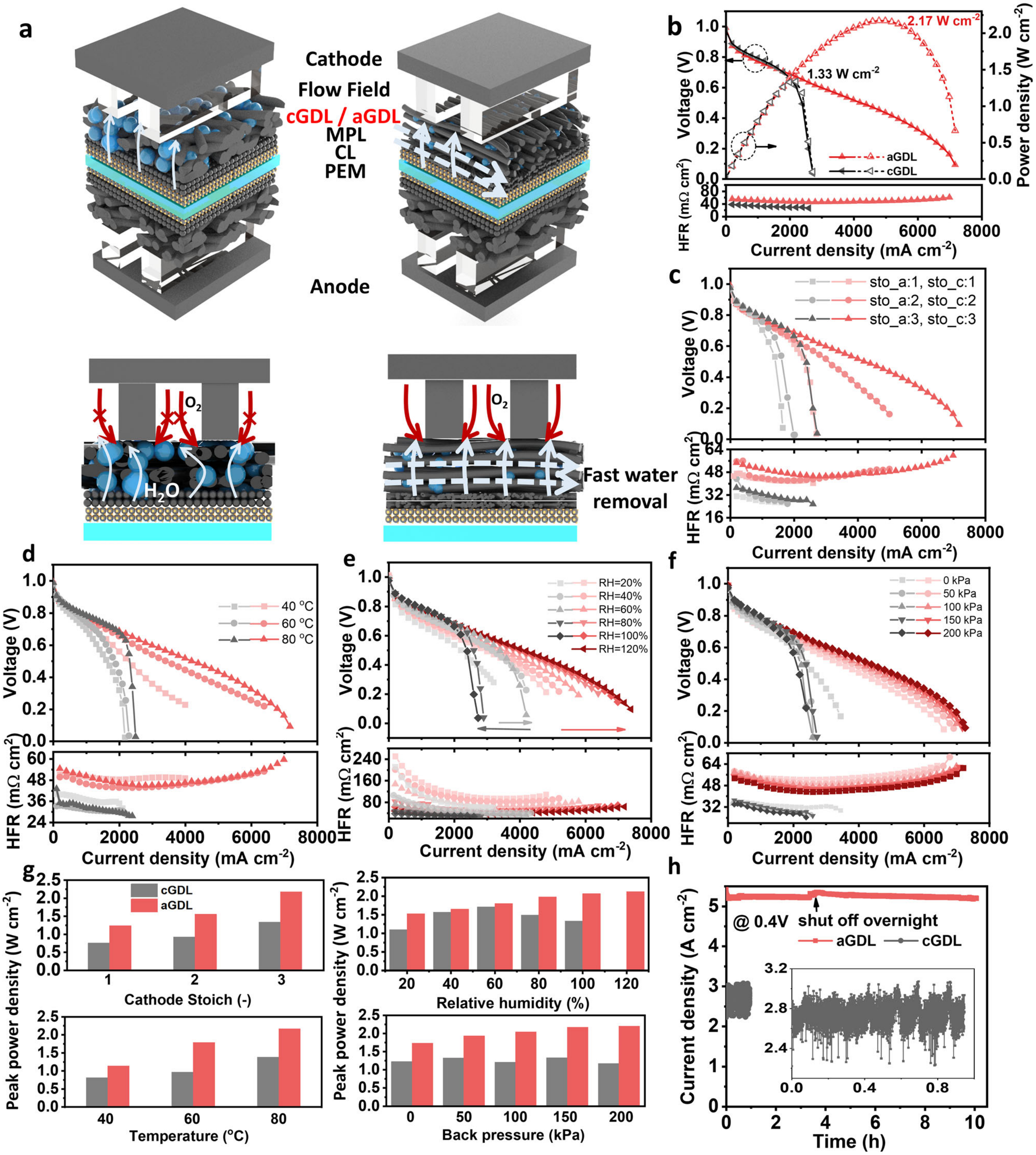

Fig. 4 | PEMFC performance comparison between aGDL and cGDL. a Schematic of the water transport pathways in cGDL and aGDL in a unit full cell and side-view of cathode half-cell. PEM proton exchange membrane, CL catalyst layer, MPL micro-porous layer. Performance (polarization curve and high-frequency resistance (HFR)) comparison at **b** standard testing condition, **c** different gas flow rates, sto_c, cathode stoichiometric number; sto_a, anode stoichiometric number, **d** different testing temperature, **e** varied humidity and **f** varied backing pressure. **g** Summary of the performance comparison in terms of peak power density. **h** Stability of PEMFC operating at 0.4 V. All the voltage is not iR corrected. Source data are provided as a Source Data file.

ohmic loss dominant region closely aligns, suggesting that GDL fiber diameter mainly affects PEMFC performance by influencing the transport process under high current densities. Activation, ohmic and concentration losses are evaluated in Supplementary Fig. 17, confirming aGDL_d3 leads to the smallest concentration loss. Therefore, the highest LCD in PEMFC with aGDL_d3 indicates the best water removal properties of the GDL. This trend can also be observed at a lower gas flow rate and different back pressures (Supplementary Fig. 18). In particular, increased GDL fiber diameter leads to enlarged pore sizes that can better remove the water.

Then, we examined the influence of MPL in PEMFCs. Commercial GDLs commonly incorporate carbon particle-based MPLs (Supplementary Fig. 19) to lower the contact resistance between the CL and GDL, and improve water transport by wicking water from the CL. Here we adopt electrospun carbon fibers as the MPL and assess its efficacy by comparing the performance of PEMFC composed of GDLs with and without MPLs. As shown in Fig. 3d, the two polarization curves deviate in both the ohmic and mass transport dominant regions. The differences in the ohmic resistance are quantified through HFR measurement, with the PEMFC using aGDL_wo showing a significantly higher HFR of 72–88 mΩ cm^2 over that of 44–56 mΩ cm^2, indicating that the adoption of an MPL can effectively reduce contact resistance. The respective activation, ohmic and concentration losses are compared in Supplementary Fig. 20, with the difference in ohmic loss being observed, and a slight increase in concentration loss for aGDL with MPL. To assess the impact of MPL on mass transport within the cell, the two PEMFCs are compared at different gas flow rates. When the cathode stoichiometric number reduces in the sequence of 3, 2, and 1, the mass transport loss in the cell with aGDL_wo is less affected by flow rates, as evidenced by the decrease in LCD from ~5500 to 4500, and 3800 mA cm^{-2}, as compared of ~7200, 5000, and 2800 mA cm^{-2} for aGDL_d3 (Supplementary Fig. 21). The result represents that the adoption of electrospun MPL leads to increased mass transport resistance, especially at a low flow rate. To strike a balance between reducing contact resistance and increasing transport resistance, MPL is adopted in the following studies.

Furthermore, we investigated the influence of different arrangements of aligned GDLs with respect to the flow channel on the PEMFC performance. Two configurations were compared: one vertical and the other parallel, as illustrated in Fig. 3a. The aGDLs are highly flexible and can be bent through the two directions, which enable a sufficient mechanical strength to be used in PEMFC (Supplementary Fig. 22). The PEMFC performance with aGDL_d3 and aGDL_parallel are compared at stoichiometric numbers of 3, 2, and 1 (Fig. 3e, and Supplementary Fig. 23). The results indicate that the PEMFC with aGDL_parallel shows a slightly increased HFR, possibly due to the reduced fiber contact with bipolar plates and the variance in electric conductivity of aGDL along different fiber orientation, as schematically illustrated in Supplementary Fig. 24. In addition, aligning the GDL's fibers parallel to the flow channel leads to increased mass transport loss, due to the tortuous path for water to transport in the under-rib region (Supplementary Fig. 25). The differences in ohmic and concentration loss are more distinctly found in Supplementary Fig. 26, that the parallel arrangement leads to increased cell ohmic and mass transport loss. Such findings are consistent with the influence of the arrangement of quadrilateral patterned perforations in our previous study[46].

Moreover, we compared the performance of GDLs with random fibers, which has the same fiber diameter as aGDL_d3. Multiple thin layers of aGDL_d3 with different displacement directions are stacked to obtain randomly arranged GDL (rGDL_d3), which shows decreased pore sizes, as has been analyzed in MIP results (Fig. 3b). The PEMFC performance shows that the mass transport loss in the polarization curve becomes more significant for the cell with rGDL_d3, indicating that the reduced pore sizes in a random arrangement lead to the reduced water drainage capability (Fig. 3f, Supplementary Figs. 27 and 28). Overall, positioning GDLs formed with aligned large fibers vertical to the flow channels enhances mass transport properties significantly.

Comparing aGDL with cGDL

To assess the potential of homemade GDLs as replacements for current commercial GDLs in practical applications, aGDL_d3 is compared with the commercial GDL (cGDL) under various operating conditions. The sample name aGDL_d3 is simplified as aGDL in this session. As shown in Fig. 4a, the commercial GDL consists of a backing layer formed with hydrophobic stochastic arranged carbon fibers and a particle-based MPL. The product water transports from the CL to the channels in the through-plane direction. In cGDL, the non-uniform and random pores usually lead to poor mass transport property, causing liquid accumulation in the pores, especially in the under-rib region[24,25,47,48]. At high operating current densities, cGDL is susceptible to water flooding, impeding O_2 diffusion to the CL and consequently deteriorating cell performance. In contrast, aGDL provides directional paths for water transport. As shown in Fig. 4a, water can more easily transport in both the through-plane and in-plane directions when the aligned GDL is vertical to the flow channel, leading to a fast water removal and preventing water flooding even at high current densities, as evidenced by polarization curves in Fig. 4b. The polarization curve of PEMFC with aGDL indicates that there is no significant mass transport loss, demonstrating an LCD of as high as ~7200 mA cm^{-2}, and a peak power density of 2.17 W cm^{-2}, which are 2.7 and 1.6 times of that with PEMFC with cGDL (~2700 mA cm^{-2} and 1.33 W cm^{-2}), at standard testing condition (Fig. 4b). The cell voltage suffers a sudden drop at the current density of around 2000 mA cm^{-2} for the cell with cGDL, representing the cGDL is severely flooded under this operating condition. HFR of the cell with cGDL is slightly lower than that of the cell with aGDL, which could be attributed to the improved contact with the particle-based MPL and better membrane hydration, as cGDL is more prone to flooding. The difference in ohmic and concentration loss is further witnessed in Supplementary Fig. 29, that cGDL leads to a significant reduced centration loss with only a slight increase in cell ohmic loss. With such a high LCD demonstrated with aGDL, further assessment of cell performance was conducted under various testing conditions, including different gas flow rates, temperature, relative humidity (RH), and back pressure.

To examine the water removal capability under even harsher operating conditions, we further reduced the stoichiometric ratios to 2/2 and 1/1, which makes it harder to remove water. Severe water flooding appears in PEMFCs with cGDL at all stoichiometric numbers. In comparison, the PEMFC with aGDL experiences water flooding only at an ultra-low flow rate with a 1/1 stoichiometric number, but still enabling an LCD 2700 mA cm^{-2}, and a peak power density of 1.23 W cm^{-2}, far higher than that with cGDL which are 1650 mA cm^{-2} and 0.75 W cm^{-2}, respectively (Fig. 4c and Supplementary Fig. 30). Moreover, the PEMFC performance is also evaluated at a lower temperature that decreased from 80 to 40 °C (Fig. 4d). Lower temperature not only leads to slower kinetics but also causes increased mass transport losses as water is prone to exist in liquid form. Unlike the cGDL-based PEMFCs, which experience flooding at 40 °C, 60 °C, and 80 °C, the aGDL-based PEMFC shows minimal mass transport losses even at 40 °C, demonstrating enhanced water removal capabilities.

Relative humidity is another important operating parameter. The performance of PEMFC with cGDL exhibits non-monotonic behavior (Fig. 4e). At a low relative humidity of 20%, insufficient membrane hydration leads to high ohmic resistance yet mitigates water flooding. With an increase in relative humidity to 40%, the cell's ohmic resistance decreases notably, resulting in an enhanced LCD. However, at RH exceeding 60%, water flooding intensifies, and mass transport loss becomes predominant. Consequently, the LCD is reduced despite the continued decline in ohmic loss. In contrast, the performance of PEMFC with aGDL exhibits a gradual improvement with increased relative humidity, which can be attributed to its improved mass transport properties that facilitate water removal even at high RH levels (e.g., 120% RH). Additionally, the acceptable HFR increase observed at an ultra-low relative humidity of 20% underscores the water retention capability of aGDL incorporating electrospun MPL.

Apart from flow rates, temperature, and RH, we also investigated the impact of back pressure on the performance of the two cells (Fig. 4f). Consistent with previous simulations and experiments[49,50], we observed decreased HFR with increasing back pressure for both cells. However, the polarization curves for PEMFC with cGDL and aGDL exhibit opposite trends with increased back pressure. The LCD of PEMFC with cGDL is highest without applying back pressure, but gradually decreases with increased back pressure. In contrast, the PEMFC curves with aGDL demonstrate a steady rise in LCD, showcasing the enhanced water removal capabilities of aGDL despite the less favorable conditions of high back pressure.

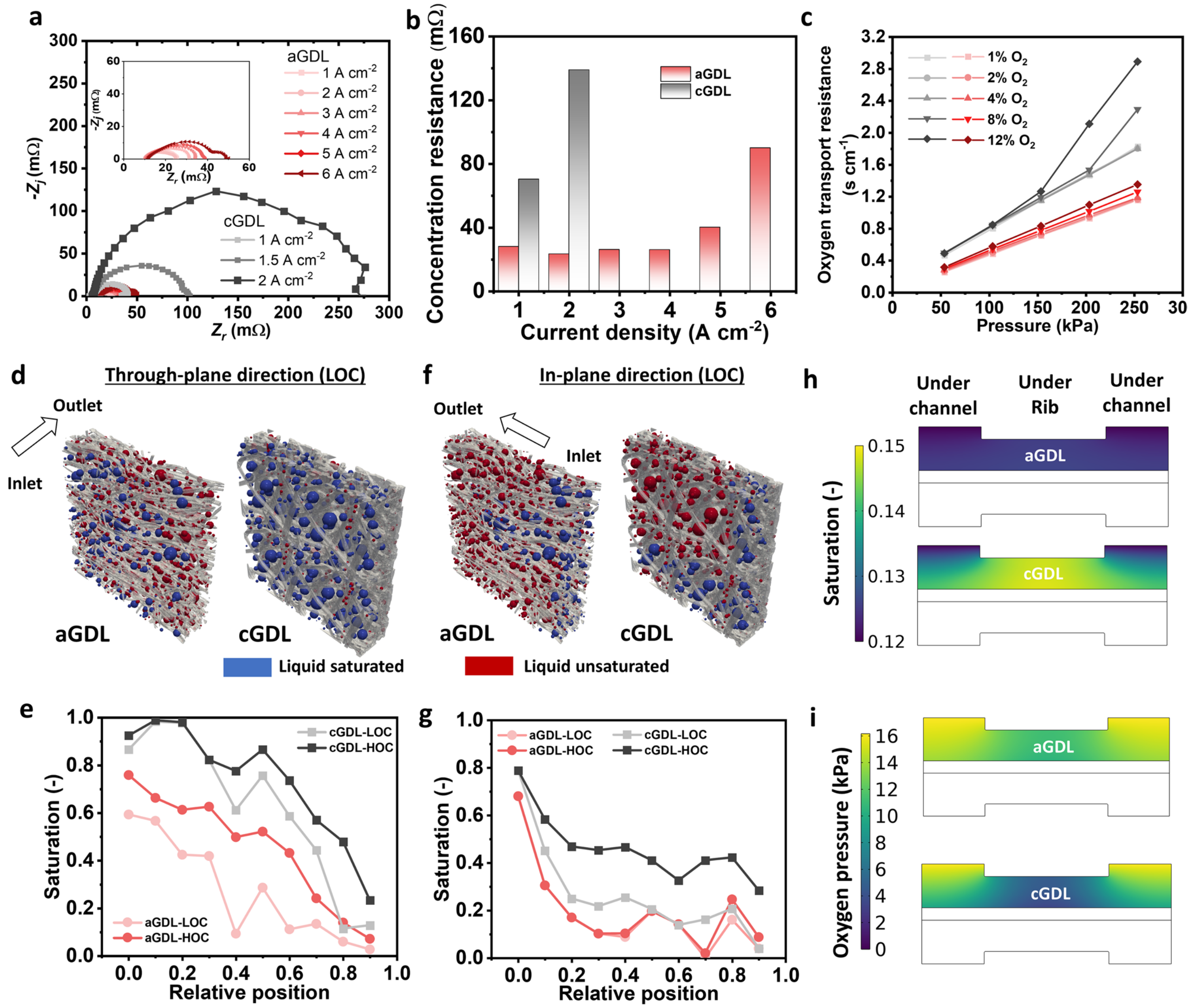

Fig. 5 | Experimental and numerical analysis of improved water drainage capabilities of aGDL compared with cGDL. a Electrochemical impedance spectroscopy (EIS) plots under different current densities. Z_j, imaginary part of the impedance; Z_r, real part of the impedance. **b** Concentration loss comparison. **c** Oxygen transport resistance comparison. Liquid water saturation distribution along **d**, **e** through-plane and **f**, **g** in-plane direction using pore network modeling. **d**, **f** Visualization of liquid saturation distribution in reconstructed GDL structure for low outlet coverage (LOC) condition. **e**, **g** Saturation curves along different directions. HOC, high outlet coverage. **h** Water saturation and **i** oxygen pressure distribution in the under-rib and under-channel region. Source data are provided as a Source Data file.

Through the comparison of cell performance across various operating conditions, we have compiled the peak power density data for all cases. The findings reveal that the performance of PEMFC with aGDL surpasses that of cGDL across all investigated operating conditions, including high/low flow rates, humidity, temperature, and back pressure settings (Fig. 4g). Furthermore, the performance achieved in our study stands out as one of the highest reported in the literature, particularly in terms of LCD versus specific flow rates, as compared in Supplementary Table 1[15,19,46,51–54]. Considering the remarkable performance demonstrated with the aGDL, we conducted further investigations on the stability of the two cells under a constant applied voltage of 0.4 V. Results reveal that the PEMFC with aGDL exhibits a stable current density of over 5000 mA cm^{-2} for 10 h. In contrast, the cell with cGDL displays significant fluctuations in current density, fluctuating between 2000 and 3000 mA cm^{-2} (Fig. 4h), suggesting that the removal of water from the cell is inadequate, leading to a non-continuous supply of oxygen.

In order to assess the anti-corrosion of the homemade GDLs, we conducted an accelerated stress test (AST). Previous experimental studies have demonstrated that conducting an AST via triangle sweep between 1.0 and 1.5 V can result in severe degradation of CLs and deterioration of the carbon materials in GDL[51]. The polarization curves obtained after 1000, 3000, and 5000 cycles reveal a gradual decrease in the peak power density of the PEMFC, accompanied by a significant increase in HFR, particularly after 3000 AST (Supplementary Fig. 30a). After 5000 AST, we disassembled the cell, replaced the catalyst coated membrane (CCM), and reused the GDL before reassembling the PEMFC. Our findings indicate that the cell performance can be restored to its initial state, and even slightly improved (Supplementary Fig. 30b), representing the high anti-corrosion properties of the as-prepared GDL. Overall, the homemade aGDL demonstrates improved performance compared to cGDLs under various operating conditions, highlighting its strong potential as a replacement for cGDLs in practical applications.

Water/gas transport analysis

To analyze mass transport losses during cell operation, Nyquist plots from Electrochemical impedance spectroscopy (EIS) tests were recorded at various operating current densities, as shown in Fig. 5a, which are fitted with an equivalent circuit model (Supplementary Fig. 31). In PEMFCs with cGDL, severe water flooding restricts EIS testing to current densities below 2 A cm^{-2}, with significant concentration loss appearing from the equivalent electric circuit simulation (Fig. 5b). Conversely, the concentration loss in cells with aGDL remains minimal at current densities ranging from 1–5 A cm^{-2}, only increasing notably at a high current density of 6 A cm^{-2}. The oxygen transport resistances (OTRs) were assessed using the LCD measures with different O_2 concentrations (Fig. 5c). It is evident that in PEMFCs with aGDL, the OTRs are significantly lower than those with cGDLs across various oxygen fractions and back pressures. OTR (R_{O_2}) can be theoretically derived by refs. 5,55,

$$R_{O_2} = \frac{L}{D_{\mathrm{eff}}} = \frac{L}{D_{\mathrm{ref}}(1-s)^3\frac{p_{\mathrm{ref}}}{p}} \tag{2}$$

where L is the thickness of porous media, S is the liquid water saturation, p is pressure, D_{eff} and D_{ref} are effective and reference diffusivity, respectively. According to Eq. 2, the OTR is affected by liquid water saturation and cell pressure. In PEMFCs with aGDL, the OTR shows a linear relationship with pressure at all oxygen concentrations, indicating that PEMFC with aGDLs remains unsusceptible to water flooding and the slightly increased slope presents a minimal rise in water saturation with increased oxygen levels. However, this linear relationship does not hold for cells with cGDL at 8 and 12% oxygen fractions, where a substantial increase is observed at higher pressure conditions, suggesting high water saturation (potentially leading to flooding) under these conditions.

To gain a comprehensive understanding of the two-phase transport processes in aGDL and cGDL, extensive pore-scale simulations were conducted and analyzed under different liquid water breakthrough conditions, specifically low outlet coverage (LOC) and high outlet coverage (HOC)[56]. Figure 5d, f provides the liquid water saturation distribution within the GDLs in the through-plane and in-plane directions under LOC. Overall, saturation demonstrates a decreasing trend from the inlets to the outlets. Notably, there are much fewer pores occupied around the inlet surface when liquid water breakthroughs happen in the outlets. Consistent with the liquid water distribution, aGDLs exhibit fewer occupied pores by liquid water in both through-plane and in-plane directions, and the saturation levels in aGDLs are consistently lower than those in cGDLs, indicating the superiority of the aGDLs with aligned fibers in both through-plane and in-plane directions under various liquid water breakthrough conditions (Fig. 5e, g). Besides the pore-scale simulation, the cell-scale simulation also confirms the superiority of aGDL, which significantly reduces the liquid water saturation and increases the oxygen pressure (Fig. 5h). Liquid water remains low in PEMFC with aGDL but accumulates in the middle (under-rib) region for PEMFC with cGDL (Fig. 5i), which leads to a significant reduction in oxygen pressure in the under-rib region and thus poorer performance.

Discussion

We identified the optimal porous GDL structure with aligned fibers using an AI-guided design strategy of GDL by integrating multi-scale modeling with Bayesian ML. The ordered GDL was successfully synthesized using a controlled electrospinning method. Through our exploration of the effects of fiber orientation, fiber diameters, presence of MPL, and GDL arrangement on PEMFC performance, it is found that fuel cells with optimized aligned GDLs positioned vertically to the flow channel exhibited an LCD of up to 7200 mA cm^{-2} and a peak power density of 2.17 W cm^{-2}, which are 2.7 times (2700 mA cm^{-2}) and 1.6 times (1.33 W cm^{-2}) higher than those achieved with commerical GDLs. The improved performance of PEMFCs with aligned GDLs was consistent across a range of test conditions, including temperatures (40–80 °C), relative humidities (20–120%), flow rates (stoichiometric ratios from 1 to 3), and back pressures (0–200 kPa). Additionally, the aligned GDL demonstrated excellent long-term resistance to flooding and corrosion. The enhanced water drainage capacity of aligned GDLs over commerical GDLs was confirmed through concentration loss measurements and oxygen transport resistance. Pore-scale and cell-scale simulations indicated that the improved through-plane and in-plane water transport enhanced water management under high current densities. The AI-guided design strategy, combined with the advanced synthesis approach, represents a leap forward in GDL technology for next-generation PEMFCs. This workflow can also be adapted to tackle complex challenges across various other fields.

Methods

Materials

PAN ($M_W = 150{,}000$), N,N-dimethylformamide (DMF, ≥99%), were obtained from Sigma-Aldrich. 1H,1H,2H,2H-PFTS, and Cobalt nitrate hexahydrate ($Co(NO_3)_2 \cdot 6H_2O$) were purchased from Aladin. All chemicals were used without any further refinement. GDLs (YSL-30T, Toray) were purchased from Suzhou Sinero Technology. The CCM consists of a 12 μm thick Gore M820.15 membrane that is coated with JM HiSPEC 9100 Pt/C catalysts. The catalyst loading of CCM was 0.12 mg Pt cm^{-2} on the anode side and 0.48 mg Pt cm^{-2} on the cathode side, supplied by Suzhou Sinero Technology.

Synthesis of the electrospun GDLs

Precursor solutions with varying concentrations of PAN, Co salt was prepared for the synthesis of MPL and backing layers. For example, to synthesize the aGDL_d3, 15 wt% precursor solution containing PAN and 1 wt% Co salt was prepared by dissolving 1.5 g of PAN and 0.1 g of Co salt in 8.4 g DMF under stirring. 10 mL of as-prepared precursor solution was pumped at a speed of 1 mL h^{-1}. A high voltage of 16 kV was applied at the tip of the nozzle with the distance between the nozzle and the collector to be ~16 cm. The ambient temperature was ~25 °C, and the relative humidity was 45–55%. Under such electrospinning conditions, the PAN/Co-based solution formed aligned microfibers, Similarly, the PAN polymer mats for the backing layers (BLs) of aGDL_d1 and aGDL_d2 were prepared with the same procedure but with a different concentration of the precursor, with the PAN concentration to be 11 wt% and 13 wt%, respectively and the PAN: Co weight ratio is kept as the same for all the precursor solutions. The polymer mat for the synthesis of MPL is prepared with an 8 wt% PAN solution and Co salt with same PAN: Co ratio, which is electrospun with a feeding rate of 0.5 mL h^{-1} in the ambience humidity of 30–40%. To prepare the GDL, the polymer mat with a thickness of around 50 μm for MPL and 250 μm for BLs were stacked together and were thermally stabilized in the air at 280 °C for 1 h and carbonized in nitrogen gas at 1100 °C for 3 h to get the desired GDLs. It was worth noting that to prepared rGDL_d3, six layers of the polymer mat for aGDL_d3 with a thickness of around 40 μm is arranged in six different orientations, as shown in Supplementary Fig. 15, and stack layer by layer to form the backing layer and on the top is fiber mat for MPL and for the synthesis of aGDL_wo, the backing layer is directly treated without stacking together with the MPL polymer mat.

Hydrophobicity treatment

The electrospun GDLs are then hydrophobic and treated with PFTS. 0.5 g PFDTES is dissolved in 50 mL ethanol and stirred for 1 h to prepare the treatment solution. The as-prepared GDLs are soaked in the solution for 1 h, followed by drying at 60 °C for 6 h.

Fuel cell testing

A laboratory-fabricated single-cell with a 2 × 2 cm^2 active area was assembled for performance evaluation. The fuel cell is equipped with bipolar plates with the typical serpentine flow channels. The anode side of the fuel cell utilized a commercial GDL with an MPL, while the cathode side employed as-prepared GDLs. Between the anode and catalyst GDLs, the CCM consisting of CLs and proton exchange membrane was used. PTFE gaskets with a thickness of 180 μm were used to seal the cell, with a uniform compression with 10 Nm torque applied.

A fuel cell test station (850 Fuel Cell Test System, Scribner) equipped with a potentiostat was used for fuel cell testing. The activation procedure of fuel cells involved a voltage-controlled ramp-in method, where the reactant flows of H_2–air were maintained at a constant rate of 1.5/1.5 NL min^{-1}, and the cell temperature was set at 80 °C with 100% relative humidity on both the anode and cathode sides, along with a back pressure of 150 kPa. During activation, the voltage was held at 0.6 and 0.4 V for 60 min. After the activation procedure, the H_2/air reactant flows were adjusted to a stoichiometric ratio of 3/3, with a minimum flow rate of 0.5/0.5 NL min^{-1}. We use the back pressure of 150 kPa, a stoichiometric ratio of 3/3 and a minimum rate of 0.5/0.5 NL min^{-1}, 100% humidity, and 80 °C temperature as the standard testing condition. To examine the influence of temperature, three different temperatures (40, 60, and 80 °C) were adjusted with other conditions set as the same. Similarly, to investigate the influence of flow rates, three flow rates were adopted which are stoichiometric ratio of 3/3 and a minimum rate of 0.5/0.5 NL min^{-1}, stoichiometric ratio of 2/2 and a minimum rate of 0.2/0.2 NL min^{-1}, and stoichiometric ratio of 1/1 and a minimum rate of 0.2/0.2 NL min^{-1}. The same is for the investigation of back pressure (0, 50, 100, 150, and 200 kPa) and humidity (20, 40, 60, 80, 100, and 120%). Polarization tests were conducted using a current sweep with a step of 0.2 A cm^{-2} to evaluate fuel cell performance. High-frequency resistance (HFR) was measured online at a frequency of 20,000 Hz during the polarization tests. EIS involved a logarithmic frequency sweep from 20,000 to 0.2 Hz with an amplitude of 5%. After testing, the cell was maintained at 0.4 V to assess its durability.

The accelerated stress test (AST)

The AST was adopted for the evaluation of the anti-corrosion and cyclability of GDL in fuel cells[51,57]. The AST was conducted with a triangle sweep circle from 1.0 to 1.5 V and a scan rate of 500 mV s^{-1}. After the first 1000 AST tests, the polarization curve was conducted at the standard testing condition. Another two 2000 AST tests were performed with the polarization curves recorded. With a total number of 5000 AST cycles, the CCM was replaced to eliminate the influence of the degradation of CCM, and the other components reused to assemble the PEMFC and were activated and tested with the standard testing conditions to investigate the degradation of GDLs.

Limiting current measurements of oxygen transport resistance

Polarization curves were measured with different dry oxygen concentrations (1%, 2%, 4%, 8%, 12%) in O_2/N_2 mixture gas to accurately acquire the limiting current densities. The tests are conducted with a constant flow rate of 0.5/0.5 NL min^{-1} at 80 °C and 100% relative humidity. The limiting current densities were recorded at the operating voltage of 0.1 V. The oxygen transport resistance is then calculated by,

$$R_{O_2} = \frac{4F}{R \cdot T_{\mathrm{cell}}} \cdot \frac{(p_{\mathrm{abs}} - p_{H_2O})}{i_{\mathrm{lim}}} \cdot x_{O_2,\mathrm{dry}} \tag{3}$$

where i_{lim} is the LCD, p_{abs} is the absolute pressure, p_{H_2O} is the water partial pressure due to the humidification, $x_{O_2,\mathrm{dry}}$ is the dry oxygen concentrations, T_{cell} is the cell temperature, F is the Faraday constant, and R is the gas constant.

Materials characterizations

To obtain the morphologies of the GDLs, scanning electron microscopy (SEM) was performed using a JEOL-7100F instrument equipped with EDS. The pore size distribution of the GDLs was measured using MIP with a Micromeritics AutoPore IV 9500 instrument, applying pressures ranging from 0.23 to 33000 psi at a temperature of 33 K. The contact angles test using a Biolin Attension Theta Flow contact angle meter to assess the wettability of the GDLs and each droplet has a volume of 3 mL. Raman spectra to compare the carbonization degree were acquired using the InVia (Renishaw) Raman spectrometer, employing a 514 nm laser as the excitation source (with a Notch Filter). The microstructure of the GDLs was obtained through X-ray CT utilizing a high-resolution setting as high as 500 nm on the ZEISS Xradia 520 system.

Numerical simulations

For pore-scale simulation, the geometry structures of GDLs are obtained from computed tomography reconstruction, which are subsequently converted to pore networks by using the subnetwork of the over-segmented watershed (SNOW) method[58]. A quasi-static invasion percolation of the pore networks is implemented to analyze the invasion sequence of the pores and throats in the two-phase (liquid water/air) transport. The two-phase flow in the pore and throat networks is governed by the capillary force. Prior to the invasion percolation process, the entire area is initially filled with air until the invasion of liquid water occurs. Different operating conditions are represented by the outlet surface coverage, i.e., high and low occupation conditions[59,60]. Following the implementation of invasion percolation, a coupled Stokes flow model is utilized to calculate the two-phase relative permeability. Anisotropic two-phase relative permeability (through-plane and in-plane directions) is determined by employing different inlet and outlet boundaries in the specified directions. The saturation distribution is analyzed by dividing the GDL into 10 segments along the given direction and subsequently calculating the average saturation level across the entire region. For cell-scale simulation, the main governing equations contain mass, momentum, and energy conservation to depict the flow in channels, while Darcy's law is used in the porous region. The conventional agglomerate model is used to describe the reaction in the cathode CL. More details can be found in references[61,62].

Bayesian optimization

BO is a recognized and effective ML technique employed for the multidimensional optimization of expensive, difficult-to-evaluate, or noisy functions. In this study, the objective of BO is to explore the input geometry parameter space for the experimental synthesis of GDLs to achieve the highest LCD. The workflow of BO in this study involves constructing a model utilizing the Gaussian process by learning from prior observations with the aid of a prior function, given by

$$P(X) = \frac{1}{\sqrt{(2\pi)^k |\sum|}} \cdot \exp\left(-\frac{1}{2}(X-\mu)^T \sum^{-1}(X-\mu)\right) \tag{4}$$

where it is easy to check $E[X] = \mu$ and $E[XX^T] = \Sigma$.

Through the optimization of the acquisition function (expected-improvement-plus), new experiments (ML-assisted multiphysical numerical simulation) are sequentially selected and conducted for the next evaluation. The results are incorporated back into the dataset to update the model, completing an optimization round.

Dataset and machine learning

A dataset consisting of 7621 fiber-based porous media structures and their corresponding transport properties is developed by using OpenPNM and Porespy packages. To ensure sufficient resolution and computational domain size, a representative volume of the generated porous media is set to 256 × 256 × 256 pixels, with each pixel representing 1 μm. The parameters of porosity, radius, and orientation are independently and uniformly distributed.

To perform pore network modeling, the representative volume matrix of the porous media needs to be transformed into a network representation. In this study, the SNOW algorithm is utilized. After extraction of pore and throat network, the single-phase Stokes flow and Fickian diffusion simulation are performed to calculate the anisotropic transport properties.

The ANN architecture began with a feature input layer of size 3, followed by three fully connected layers with 128, 256, and 512 neurons, respectively, each succeeded by a ReLU activation layer. The final fully connected layer matched the dimensionality of the target data, and the network concluded with a regression layer to perform the necessary predictions. The dataset was divided into training (70%), validation (15%), and test (15%) sets. The training process employed the Adam optimizer, set up a maximum of 50 epochs, a mini-batch size of 128, and an initial learning rate of 0.001. L2 regularization was used to avoid overfitting.

Reporting summary

Further information on research design is available in the Nature Portfolio Reporting Summary linked to this article.

Data availability

The dataset developed and used for this study is available at deposited in the Zenodo repository under an MIT license at https://doi.org/10.5281/zenodo.15622653[63]. Source data are provided with this paper.

Code availability

The code and scripts developed and used for this study are available in the Zenodo repository under a MIT license at https://doi.org/10.5281/zenodo.15622653[63], including the ANN model and the BO algorithm.

References

1. Adams, J. *DOE H2 Heavy Duty Truck Targets*. https://www.energy.gov/sites/prod/files/2020/02/f71/fcto-compressed-gas-storage-workshop-2020-adams.pdf. (2020).
2. Wang, Y., Pang, Y., Xu, H., Martinez, A. & Chen, K. S. PEM Fuel cell and electrolysis cell technologies and hydrogen infrastructure development–a review. *Energy Environ. Sci.* **15**, 2288–2328 (2022).
3. Gittleman, C. S., Jia, H., De Castro, E. S., Chisholm, C. R. & Kim, Y. S. Proton conductors for heavy-duty vehicle fuel cells. *Joule* **5**, 1660–1677 (2021).
4. Kempler, P. A., Slack, J. J. & Baker, A. M. Research priorities for seasonal energy storage using electrolyzers and fuel cells. *Joule* **6**, 280–285 (2022).
5. Liang, J., Li, Y., Wang, R. & Jiang, J. Cross-dimensional model of the oxygen transport behavior in low-Pt proton exchange membrane fuel cells. *Chem. Eng. J.* **400**, 125796 (2020).
6. Adams, J. (ed Compressed Gas Storage for Medium and Heavy Duty Transportation Workshop) (2020).
7. Cullen, D. A. et al. New roads and challenges for fuel cells in heavy-duty transportation. *Nat. Energy* **6**, 462–474 (2021).
8. Csoklich, C., Xu, H., Marone, F., Schmidt, T. J. & Büchi, F. N. Laser structured gas diffusion layers for improved water transport and fuel cell performance. *ACS Appl. Energy Mater.* **4**, 12808–12818 (2021).
9. Lee, C. et al. Grooved electrodes for high-power-density fuel cells. *Nat. Energy* **8**, 685–694 (2023).
10. Peng, B. et al. Embedded oxide clusters stabilize sub-2 nm Pt nanoparticles for highly durable fuel cells. *Nat. Catal.* **7**, 818–828 (2024).
11. You, J. et al. Insight into oxygen diffusion mechanism in ionomer film on catalyst surface with varying perfluorosulfonic acid and water contents. *J. Mater. Chem. A* **12**, 7248–7256 (2024).
12. Jiao, K. & Li, X. Water transport in polymer electrolyte membrane fuel cells. *Prog. energy Combust. Sci.* **37**, 221–291 (2011).
13. Duan, Z. & Xiao, P. Simulation of potential-dependent activation energies in electrocatalysis: mechanism of O–O bond formation on RuO2. *J. Phys. Chem. C.* **125**, 15243–15250 (2021).
14. Ozden, A., Shahgaldi, S., Li, X. & Hamdullahpur, F. A review of gas diffusion layers for proton exchange membrane fuel cells—With a focus on characteristics, characterization techniques, materials and designs. *Prog. Energy Combust. Sci.* **74**, 50–102 (2019).
15. Wen, Q. et al. Janus gas diffusion layer for enhanced water management in proton exchange membrane fuel cells (PEMFCs). *ACS Energy Lett.* **7**, 3900–3909 (2022).
16. Gerteisen, D., Heilmann, T. & Ziegler, C. Enhancing liquid water transport by laser perforation of a GDL in a PEM fuel cell. *J. Power Sources* **177**, 348–354 (2008).
17. Gerteisen, D. & Sadeler, C. Stability and performance improvement of a polymer electrolyte membrane fuel cell stack by laser perforation of gas diffusion layers. *J. Power Sources* **195**, 5252–5257 (2010).
18. Tongsh, C. et al. Fuel cell stack redesign and component integration radically increase power density. *Joule* **8**, 175–192 (2024).
19. Csoklich, C., Schmidt, T. J. & Büchi, F. N. High-performance gas diffusion layers with added deterministic structures. *Energy Environ. Sci.* **15**, 1293–1306 (2022).
20. Calili-Cankir, F. et al. Patterned hydrophobic gas diffusion layers for enhanced water management in polymer electrolyte fuel cells. *Chem. Eng. J.* **484**, 149711 (2024).
21. Forner-Cuenca, A. et al. Advanced water management in PEFCs: diffusion layers with patterned wettability II. Measurement of capillary pressure characteristic with neutron and synchrotron imaging. *J. Electrochem. Soc.* **163**, F1038 (2016).
22. Forner-Cuenca, A. et al. Engineered water highways in fuel cells: radiation grafting of gas diffusion layers. *Adv. Mater.* **27**, 6317–6322 (2015).
23. Cai, F., Cai, S. & Tu, Z. Proton exchange membrane fuel cell (PEMFC) operation in high current density (HCD): problem, progress and perspective. *Energy Convers. Manag.* **307**, 118348 (2024).
24. Nagai, Y. et al. Improving water management in fuel cells through microporous layer modifications: Fast operando tomographic imaging of liquid water. *J. Power Sources* **435**, 226809 (2019).
25. Muirhead, D. et al. Liquid water saturation and oxygen transport resistance in polymer electrolyte membrane fuel cell gas diffusion layers. *Electrochim. Acta* **274**, 250–265 (2018).
26. Csoklich, C., Steim, R., Marone, F., Schmidt, T. J. & Buchi, F. N. Gas diffusion layers with deterministic structure for high performance polymer electrolyte fuel cells. *ACS Appl. Mater. Interfaces* **13**, 9908–9918 (2021).
27. Wang, Z. et al. Rational design of perovskite ferrites as high-performance proton-conducting fuel cell cathodes. *Nat. Catal.* **5**, 777–787 (2022).
28. Jiang, Z. et al. Machine-learning-revealed statistics of the particle-carbon/binder detachment in lithium-ion battery cathodes. *Nat. Commun.* **11**, 2310 (2020).
29. Wang, Y. D. et al. Large-scale physically accurate modelling of real proton exchange membrane fuel cell with deep learning. *Nat. Commun.* **14**, 745 (2023).
30. Ding, R. et al. Designing AI-aided analysis and prediction models for nonprecious metal electrocatalyst-based proton-exchange membrane fuel cells. *Angew. Chem. Int. Ed.***59**, 19175–19183 (2020).
31. Rui, Z. et al. Design of proton exchange membranes with high durability for fuel cells: From the perspective of machine learning. *J. Membr. Sci.* **683**, 121831 (2023).
32. Ding, R. et al. Application of machine learning in optimizing proton exchange membrane fuel cells: a review. *Energy AI* **9**, 100170 (2022).
33. Omongos, R. L., Galvez-Aranda, D. E., Zanotto, F. M., Vernes, A. & Franco, A. A. Machine learning-driven optimization of gas diffusion

layer microstructure for PEM fuel cells. *J. Power Sources* **625**, 235583 (2025).
34. Yu, J., Duquesnoy, M., Liu, C. & Franco, A. A. Optimization of the microstructure of carbon felt electrodes by applying the lattice Boltzmann method and Bayesian optimizer. *J. Power Sources* **575**, 233182 (2023).
35. Hao, J. et al. Structural gradient optimization of diffusion layer based on finite data mapping method for PEMFC performance improvement. *Int. J. Heat. Mass Transf.* **220**, 124948 (2024).
36. Wang, J. et al. Integration of multi-physics and machine learning-based surrogate modelling approaches for multi-objective optimization of deformed GDL of PEM fuel cells. *Energy AI* **14**, 100261 (2023).
37. Okuzaki, H., Takahashi, T., Miyajima, N., Suzuki, Y. & Kuwabara, T. Spontaneous formation of poly (p-phenylenevinylene) nanofiber yarns through electrospinning of a precursor. *Macromolecules* **39**, 4276–4278 (2006).
38. Sun, J., Wu, M., Jiang, H., Fan, X. & Zhao, T. Advances in the design and fabrication of high-performance flow battery electrodes for renewable energy storage. *Adv. Appl. Energy* **2**, 100016 (2021).
39. Sun, J. et al. Aligned hierarchical electrodes for high-performance aqueous redox flow battery. *Appl. Energy* **271**, 115235 (2020).
40. Thambiliyagodage, C. J., Ulrich, S., Araujo, P. & Bakker, M. G. Catalytic graphitization in nanocast carbon monoliths by iron, cobalt and nickel nanoparticles. *Carbon* **134**, 452–463 (2018).
41. Goldie, S. J., Jiang, S. & Coleman, K. S. Cobalt nanoparticle catalysed graphitization and the effect of metal precursor decomposition temperature. *Mater. Adv.* **2**, 3353–3361 (2021).
42. Sun, X. et al. Robust preparation of flexibly super-hydrophobic carbon fiber membrane by electrospinning for efficient oil-water separation in harsh environments. *Carbon* **182**, 11–22 (2021).
43. Dresselhaus, M., Jorio, A. & Saito, R. Characterizing graphene, graphite, and carbon nanotubes by Raman spectroscopy. *Annu. Rev. Condens. Matter Phys.* **1**, 89–108 (2010).
44. Peng, H. et al. Highly electrically conductive graphene papers via catalytic graphitization. *Nano Res.* **15**, 4902–4908 (2022).
45. Chen, L., Fang, T., Song, C., Li, H. & Hu, J. Catalytic graphitization of boron on the fabrication of high-performance carbon papers for gas diffusion layers in PEMFCs. *Catal. Commun.* **157**, 106332 (2021).
46. Lin, P., Sun, J., He, C., Wu, M. & Zhao, T. Quadrilateral-patterned perforated gas diffusion layers boost the performance of fuel cells. *ACS Energy Lett.* **9**, 1710–1716 (2024).
47. Oberholzer, P. & Boillat, P. Local characterization of PEFCs by differential cells: systematic variations of current and asymmetric relative humidity. *J. Electrochem. Soc.* **161**, F139 (2013).
48. Eller, J., Marone, F. & Büchi, F. N. Operando sub-second tomographic imaging of water in PEFC gas diffusion layers. *ECS Trans.* **69**, 523 (2015).
49. Lu, J., Wei, G., Zhu, F., Yan, X. & Zhang, J. Pressure effect on the PEMFC performance. *Fuel Cells* **19**, 211–220 (2019).
50. Zhang, Q., Lin, R., Técher, L. & Cui, X. Experimental study of variable operating parameters effects on overall PEMFC performance and spatial performance distribution. *Energy* **115**, 550–560 (2016).
51. Wen, Q. et al. A recyclable standalone microporous layer with interpenetrating network for sustainable fuel cells. *Adv. Mater.* **35**, 2301504 (2023).
52. Trogadas, P. et al. A nature-inspired solution for water management in flow fields for electrochemical devices. *Energy Environ. Sci.* **17**, 2007–2017 (2024).
53. Simon, C., Endres, J., Nefzger-Loders, B., Wilhelm, F. & Gasteiger, H. A. Interaction of pore size and hydrophobicity/hydrophilicity for improved oxygen and water transport through microporous layers. *J. Electrochem. Soc.* **166**, F1022 (2019).
54. Jang, S. et al. Enhanced water management of three-dimensional graphene-Ni foam with patterned wettability in a polymer electrolyte membrane fuel cell. *ACS Sustain. Chem. Eng.* **7**, 15487–15494 (2019).
55. Vetter, R. & Schumacher, J. O. Experimental parameter uncertainty in proton exchange membrane fuel cell modeling. Part I: scatter in material parameterization. *J. Power Sources* **438**, 227018 (2019).
56. Guan, R., Shrestha, P., Lee, J. K. & Bazylak, A. Determining local transport properties of gas diffusion layer land-channel regions via pore network modelling. *J. Power Sources* **562**, 232770 (2023).
57. Team U. D. F. C. T. *Cell Component Accelerated Stress Test and Polarization Curve Protocols for PEM Fuel Cells* (Office of Energy Efficiency & Renewable Energy, 2013).
58. Gostick, J. T. Versatile and efficient pore network extraction method using marker-based watershed segmentation. *Phys. Rev. E* **96**, 023307 (2017).
59. Lee, J., Lee, C. & Bazylak, A. Pore network modelling to enhance liquid water transport through porous transport layers for polymer electrolyte membrane electrolyzers. *J. Power Sources* **437**, 226910 (2019).
60. Fazeli, M., Hinebaugh, J. & Bazylak, A. Investigating inlet condition effects on PEMFC GDL liquid water transport through pore network modeling. *J. Electrochem. Soc.* **162**, F661 (2015).
61. Lin, P. Z., Sun, J., Shao, M. H., Wu, M. C. & Zhao, T. S. Modeling proton exchange membrane fuel cells with fiber-based microporous layers. *Int. J. Heat. Mass Transf.* **198**, 123398 (2022).
62. Fuel Cell & Electrolyzer Module User's Guide. Retrieved from https://doc.comsol.com/6.2/docserver/#!/com.comsol.help.fce/html_FuelCellAndElectrolyzerModuleManual.html.
63. Sun, J. et al. Artificial-intelligence-guided design of ordered gas diffusion layers for high-performing fuel cells via Bayesian machine learning, pengzhulin/AI_guided_GDL_PEMFCn, https://doi.org/10.5281/zenodo.15622653, (2025).

Acknowledgements

This work described in this paper was supported by grant from the Research Grants Council of the Hong Kong Special Administrative Region, China (C6011-20G, and JLFS/P-602/24), Guangdong Basic and Applied Basic Research Foundation (No. 2023B1515120022), Guangdong Major Project of Basic and Applied Basic Research (2023B0303000002), and high level of special funds (G03034K001).

Author contributions

T.Z., J.S., and. P.L. conceived the study; P.L. conducted the numerical simulation; J.S. synthesized the GDL; J.S., P.L., L.Z., Y.J., C.X., and Z.L. tested the PEMFC performance. J.S., P.L., Z.G., Q.J., J.R., L.P., X.X., and L.W. analyzed the results. J.S. and P.L. drafted the manuscript and all co-authors reviewed the manuscript.

Competing interests

The authors declare no competing interests.

Additional information

Supplementary information The online version contains supplementary material available at https://doi.org/10.1038/s41467-025-61794-y.

Correspondence and requests for materials should be addressed to Tianshou Zhao.

Peer review information *Nature Communications* thanks Xiaochun Zhou and the other anonymous reviewer(s) for their contribution to the peer review of this work. A peer review file is available.

Reprints and permissions information is available at http://www.nature.com/reprints